

Tuning jammed frictionless disk packings from isostatic to hyperstatic

Carl F. Schreck,¹ Corey S. O'Hern,^{2,1} and Leonardo E. Silbert³

¹*Department of Physics, Yale University, New Haven, Connecticut 06520-8120, USA*

²*Department of Mechanical Engineering & Materials Science, Yale University, New Haven, Connecticut 06520-8260, USA*

³*Department of Physics, Southern Illinois University, Carbondale, Illinois 62901, USA*

(Received 13 July 2010; revised manuscript received 27 May 2011; published 27 July 2011)

We perform extensive computational studies of two-dimensional static bidisperse disk packings using two distinct packing-generation protocols. The first involves thermally quenching equilibrated liquid configurations to zero temperature over a range of thermal quench rates r and initial packing fractions followed by compression and decompression in small steps to reach packing fractions ϕ_J at jamming onset. For the second, we seed the system with initial configurations that promote micro- and macrophase-separated packings followed by compression and decompression to ϕ_J . Using these protocols, we generate more than 10^4 static packings over a wide range of packing fraction, contact number, and compositional and positional order. We find that disordered, *isostatic* packings exist over a finite range of packing fractions in the large-system limit. In agreement with previous calculations, the most dilute mechanically stable packings with $\phi_{\min} \approx 0.84$ are obtained for $r > r^*$, where r^* is the rate above which ϕ_J is insensitive to rate. We further compare the structural and mechanical properties of isostatic versus hyperstatic packings. The structural characterizations include the contact number, several order parameters, and mixing ratios of the large and small particles. We find that the isostatic packings are positionally and compositionally disordered (with only small changes in a number of order parameters), whereas bond-orientational and compositional order increase strongly with contact number for hyperstatic packings. In addition, we calculate the static shear modulus and normal mode frequencies (in the harmonic approximation) of the static packings to understand the extent to which the mechanical properties of disordered, isostatic packings differ from partially ordered packings. We find that the mechanical properties of the packings change *continuously* as the contact number increases from isostatic to hyperstatic.

DOI: [10.1103/PhysRevE.84.011305](https://doi.org/10.1103/PhysRevE.84.011305)

PACS number(s): 83.80.Fg, 61.43.-j, 62.20.-x, 64.75.Gh

I. INTRODUCTION

The ability to enumerate and classify all of the mechanically stable (MS) packings of frictionless particles is important for understanding glass transitions [1] in atomic, molecular, and colloidal systems and the structural and mechanical properties of particulate materials such as granular media, foams, and emulsions. For example, if all MS packings in a given system are known, one can measure accurately the frequency with which each MS packing occurs and determine how the packing frequencies and materials properties depend on the preparation history [2,3]. Further, MS packing frequencies are important for identifying the appropriate statistical mechanical ensemble for weakly perturbed granular materials [4]. However, since the number of MS packings grows exponentially with the number of particles [5], exact enumeration of static packings is prohibitive for even modest system sizes [6]. Thus, one of the most important outstanding questions in the area of disordered particulate materials is determining how the packing-generation protocol influences the distribution of MS packings and their structural and mechanical properties.

Previous work has suggested that the positional order of MS packings of frictionless spheres increases monotonically with packing fraction and contact number in dense packings [7,8]. However, the MS packings in previous studies were created using monodisperse systems, which are prone to crystallization [9], and prepared using the Lubachevsky-Stillingier compression algorithm [10], which is a thermalized packing-generation protocol. In addition, these prior studies did not distinguish the distribution of isostatic MS packings (in which the number of degrees of freedom matches the number of constraints

[11]) from the distribution of hyperstatic packings (with more contacts than degrees of freedom). Later work characterized bidisperse systems, which are less prone to crystallization, but focused on microphase-separated states, not amorphous, isostatic packings [12]. However, more recent simulation studies of 3D frictionless, spherical particles have pointed out that amorphous, isostatic packings can exist over a finite range of packing fraction, with only weak correlations between positional order and packing fraction [13–15]. Moreover, simulations [16] and experiments [17] on two-dimensional systems also suggest a finite range of jamming onsets rather than a single packing fraction in the large-system limit.

Further, the body of work on jammed particulate systems has emphasized the concept of point J, i.e., that there is a single packing fraction at which jamming occurs in the large-system limit [18,19]. Since amorphous, isostatic packings can exist over a finite range of packing fractions, the onset of jamming should not be classified as a point in the jamming phase diagram but rather as a region of finite extent [13]. It has also been argued that the wide distribution of packing fractions at which the onset of jamming occurs in small periodic systems [18] is related to the finite range of packing fractions over which amorphous, isostatic packings occur in the large-system limit [20]. However, it has not been proved that these two effects are directly connected.

A number of overarching questions related to the connection between structural order, isostaticity, and material properties of static packings remain open. For example, can isostatic or nearly isostatic packings possess significant positional order and, if so, what are the fundamental differences

in the normal modes and mechanical properties between those that do and do not possess significant positional order? This question is particularly important since recent studies have emphasized that *amorphous*, isostatic packings possess an excess of low-frequency normal modes [21,22] over that for harmonic, ordered solids.

In addition, previous work has drawn a strong contrast between amorphous packings and configurations with crystalline order [23]. However, how do the structural and mechanical properties of amorphous versus partially ordered particulate systems differ? For example, it is possible that the amorphous regions in the interstices between ordered domains in partially crystalline materials dominate the structural and mechanical properties, in which case their properties would be similar to amorphous packings. At the very least, one would assume that there is not a strong difference between the mechanical properties of isostatic and only slightly hyperstatic packings that possess significant positional order.

In this article, we describe extensive computer simulations of collections of frictionless disks with repulsive contact interactions to address two important, open questions: (i) What is the range of packing fractions over which amorphous, isostatic static packings occur with similar structural and mechanical properties? and (ii) How do the structural and mechanical properties of static packings change with the deviation in the contact number at jamming onset from the isostatic value, $z_J - z_{\text{iso}}$ [24]? Using two distinct packing-generation protocols, we construct scatter plots for more than 10^4 static packings characterized by the contact number, packing fraction, measures of positional order, and mechanical properties. The first protocol involves thermally quenching equilibrated liquid configurations to zero temperature over a range of thermal quench rates r followed by compression and decompression in small steps to reach packing fractions ϕ_J at jamming onset. For the second, we seed the system with initial configurations that promote micro- and macrophase-separated packings followed by compression and decompression to ϕ_J .

Our main results are fourfold: (i) In agreement with previous studies [13,15,16], we find that isostatic, disordered packings exist over a finite range of packing fraction in the large-system limit, with similar structural and mechanical properties. (ii) We find that the most dilute packings with $\phi_{\text{min}} \approx 0.84$ are generated when $r > r^*$, where r^* is the rate above which ϕ_J is insensitive to rate. In contrast, the most compact MS packings generated depend sensitively on quench rate and boundary conditions. (iii) The amorphous, isostatic packings coexist with an abundance of hyperstatic and microphase- and macrophase-separated packings. (iv) When considering the full ensemble of static frictionless MS packings, the packings possess structural and mechanical properties that span a continuous range from amorphous to partially ordered to ordered.

The remainder of the manuscript is organized as follows. In Sec. II, we describe the computational system we consider and the two protocols we employ to generate static frictionless disk packings. In Secs. III and IV, we present our results, which include characterizations of the structural (packing fraction, contact number, and several order parameters to detect positional and compositional order) and mechanical

(shear modulus and eigenvalues of the dynamical matrix in the harmonic approximation [3]) properties of more than 10^4 static packings and comparisons of these properties for isostatic and hyperstatic configurations. Finally, in Sec. V, we provide our conclusions and promising future research directions.

II. PACKING-GENERATION PROTOCOLS

We focus on well-characterized two-dimensional systems composed of N bidisperse disks (50-50 by number), each of mass m , with diameter ratio $d = \sigma_l/\sigma_s = 1.4$ [12,18,25], within square, periodic simulation cells with side length L . We consider frictionless particles that interact through the finite-range, purely repulsive linear spring potential. The total potential energy per particle is given by

$$V = \frac{\epsilon}{2N} \sum_{i>j} \left(1 - \frac{r_{ij}}{\sigma_{ij}}\right)^2 \Theta\left(1 - \frac{r_{ij}}{\sigma_{ij}}\right), \quad (1)$$

where r_{ij} is the center-to-center separation between disks i and j , ϵ is the characteristic energy scale of the interaction, $\Theta(x)$ is the Heaviside function, and $\sigma_{ij} = (\sigma_i + \sigma_j)/2$ is the average diameter. We simulated a range of system sizes from $N = 256$ to 8192 particles to assess finite-size effects. Energy, temperature, length, and time scales are measured in units of ϵ , ϵ/k_B , σ_s , and $\sigma_s\sqrt{m/\epsilon}$, respectively, where k_B is the Boltzmann constant.

The packing fraction ϕ_J at which jamming occurs and the structural and mechanical properties of static packings can depend strongly on the packing-generation protocol employed [14]. Our goal is to generate static frictionless MS packings that span the range of contact numbers from the isostatic value $z_{\text{iso}} = 4$ to the hexagonal crystal value $z_{\text{xtal}} = 6$ and the range of positional order from amorphous to phase separated and from partially crystalline to crystalline states. To accomplish this, we investigate two distinct classes of packing-generation protocols: (i) thermal quenching from liquid initial conditions coupled with compression and decompression steps, which typically generates amorphous configurations and (ii) compression and decompression steps from initial conditions that promote micro- or macrophase separation [26].

A. Protocol 1: Thermal quenching from liquid initial conditions

In this algorithm, we prepare equilibrated, liquid configurations at high temperature $T_0 = 10^{-3}$ and in molecular dynamics (MD) simulations quench them to a very low final temperature $T_f = 10^{-16} \simeq 0$ at fixed packing fraction $\phi_i^{\text{min}} \leq \phi_i \leq \phi_i^{\text{max}}$ over a time interval t by rescaling the particle velocities so the kinetic temperature $T = N^{-1} \sum_i m v_i^2/2$ obeys

$$T(t) = T_0 e^{-rt}, \quad (2)$$

where r is the thermal quench rate, which is varied over six orders of magnitude $10^{-6} \leq r \leq 1$. The range of initial packing fractions from $\phi_i^{\text{min}} = 0.835$ to $\phi_i^{\text{max}} = 0.856$ was chosen so we averaged over the most probable MS packings at each thermal quench rate studied. We generated 300 equilibrated, independent liquid configurations at T_0 at each ϕ_i by writing out configurations every 10τ , where τ is a decay

time obtained from the self-intermediate scattering function at wave numbers corresponding to the first peak in the structure factor [27].

After reaching a local potential energy minimum at each initial packing fraction ϕ_i and thermal quench rate r , we input the configurations into an “athermal” algorithm (“packing finder”) that searches for the nearest static packing in configuration space with infinitesimal particle overlaps. The algorithm has been described in detail in previous work [3]. Briefly, we successively increase or decrease the diameters of the grains (while maintaining the diameter ratio d), with each compression or decompression step followed by conjugate gradient minimization of V . The system is decompressed when the total potential energy per particle at a local minimum is nonzero, i.e., there are finite particle overlaps. If the potential energy of the system is zero and gaps exist between particles, the system is compressed. The increment by which the packing fraction is changed at each compression or decompression step is gradually decreased. Numerical details of the algorithm are the same as in Ref. [3]. When this algorithm terminates, we obtain a static packing defined by the particle positions $\{\vec{r}_1, \vec{r}_2, \dots, \vec{r}_N\}$ and packing fraction ϕ_J . Since we use an energy tolerance (per particle) $V_{\text{tol}}/\epsilon = 10^{-16}$ for the termination of the energy minimization and compression/decompression scheme in the packing finder, the positions and packing fraction at jamming are extremely accurate with errors at one part in 10^8 .

B. Protocol 2: Compression and decompression steps from initial conditions that promote order

We will see below in Sec. III that Protocol 1 produces disordered, isostatic packings. Thus, we seek an algorithm that will generate static packings with significant positional and compositional order. To bias the system toward micro- and macrophase-separated configurations, we seed the packing finder with particular sets of initial conditions. We first divided the simulation box into $s \times s$ equal-sized partitions, where s is an even integer that ranged from 2 to 26, and placed approximately N/s^2 large or small particles in alternating partitions to create a checkerboard-like pattern. The particles were placed randomly in each partition. The initial configuration is then input into the packing finder to yield a static packing. In the large s limit, we expect amorphous static packings, while at intermediate and small s , we expect micro- and macrophase-separated packings. To generate static hexagonal crystalline packings [28] with $\phi_{\text{xtal}} = \pi/2\sqrt{3}$, we divided the simulation box into two partitions and placed the large and small particles on a hexagonal lattice in a region with area $A_L = d^2/(1+d^2)$ and $1 - A_L$, respectively, and then applied the packing finder.

III. STRUCTURAL PROPERTIES

After generating static packings using the two packing-generation protocols described above, we contrast them by calculating several structural and mechanical properties. The structural characterizations include the packing fraction, contact number, and compositional and positional order

parameters. For the packing fraction at jamming onset, we calculate

$$\phi_J = \frac{N\pi}{8} \left(\frac{\sigma_s}{L} \right)^2 (1 + d^2), \quad (3)$$

including all N particles. For the contact number at jamming, we sum up all overlapping pairs ($r_{ij} \leq \sigma_{ij}$) of particles, $z_J = N_c/N'$, where $N' = N - N_r$, N_r is the number of rattler particles with fewer than three contacts, and N_c only includes overlapping pairs among the N' particles within the “true” contact network. It is crucial to perform an error analysis on the contact number z_J , which is described in Appendix A.

A. Packing fraction

We show results for the average packing fraction $\langle \phi_J \rangle$ versus thermal quench rate r over nearly six orders of magnitude obtained from Protocol 1 in Fig. 1. For large rates $r > r^* \approx 0.03$, the average packing fraction $\langle \phi_J \rangle \rightarrow 0.842$ is independent of rate, which agrees with studies that employ athermal compression/decompression packing-generation algorithms [2, 18]. For $r < r^*$, $\langle \phi_J \rangle$ increases approximately as $[\log_{10}(r^*/r)]^{0.5}$ with decreasing rate. In Appendix III B, we will show that all packings used to present the data in Fig. 1 are (very nearly) mechanically stable and isostatic. Since $\langle \phi_J \rangle$ increases so slowly, we are not able to approach ϕ_{xtal} using Protocol 1. Using an extrapolation, we estimate that rates below 10^{-45} are required to reach ϕ_{xtal} , and thus we employed Protocol 2, not Protocol 1, to generate compositionally and positionally ordered packings. We also show in Fig. 1 that the system-size dependence of $\langle \phi_J \rangle$ is weak. The faster rates show some system-size dependence, but we know from previous studies that $\langle \phi_J \rangle \approx 0.842$ in the infinite quench and large-system limits [18].

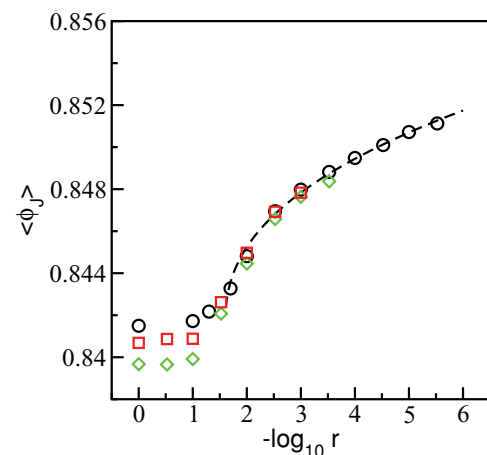


FIG. 1. (Color online) Average packing fraction $\langle \phi_J \rangle$ obtained from Protocol 1 as a function of the negative logarithm of the thermal quench rate r for $N = 256$ (circles), 512 (squares), and 1024 (diamonds). Data points at each rate represent an average over typically 300 static packings. The dashed line shows the scaling $\langle \phi_J \rangle \sim [\log_{10}(r^*/r)]^\mu$, where $\mu \sim 0.5$ and $r^* \approx 0.03$ is the thermal quench rate above which $\langle \phi_J \rangle \approx 0.842$ is independent of r (for the large N data).

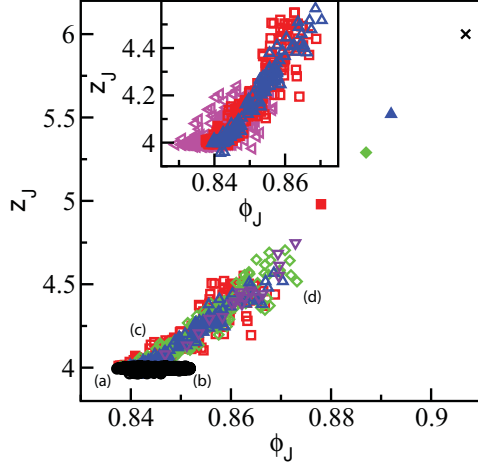


FIG. 2. (Color online) Scatter plot of the contact number z_J versus the packing fraction at jamming onset ϕ_J . The open circles indicate static packings that were generated using Protocol 1 for $N = 1024$, while all other symbols indicate static packings generated using Protocol 2. The open squares, diamonds, upward triangles, and downward triangles correspond to $N = 1024, 2048, 4096, 8192$, respectively. The solid squares, diamonds, and triangles correspond to $N = 1024, 2048$, and 4096 , respectively, for the systems with two partitions and initial crystal lattice positions. The black cross indicates the values $z_J = 6$ and $\phi_J = \pi/2\sqrt{3}$ for the hexagonal crystal. The labels (a)–(d) correspond to the images in Fig. 3. The inset shows the system-size dependence for systems with two partitions and random initial positions at $N = 256$ (leftward triangles), 1024 (squares), and 4096 (upward triangles).

B. Contact number

In Fig. 2, we display a scatter plot of the contact number z_J versus ϕ_J for all static packings (where the contact number is insensitive to the definition of “contact”) generated using Protocols 1 and 2. (See Appendix A for a discussion of the sensitivity of the contact number on the definition of contacting particles.) Figure 2 shows several compelling features. First, nearly all of the static packings obtained from Protocol 1 (open circles) are isostatic with $z_J = 4$, but they occur over a range of packing fractions $\phi_{\min} \leq \phi_J \leq \phi_{\max}(r)$, where $\phi_{\min} = 0.837$ and $\phi_{\max}(r = 10^{-6}) = 0.853$. In Appendix D, we show that all packings generated from Protocol 1 are (very nearly) mechanically stable, and thus $z = z_{\text{iso}}$ defines isostaticity. Clearly, ϕ_{\max} will increase with decreasing thermal quench r ; however, further studies are required to determine whether static packings with $\phi_J > \phi_{\max}(r = 10^{-6})$ are isostatic. Second, we find a cluster of data points for Protocol 2, for which the average z_J is strongly correlated—varying roughly linearly—with ϕ_J . The cluster originates near $\phi_J \approx 0.84$, $z_J = z_{\text{iso}} = 4$. In the inset to Fig. 2, we show that the width of the cluster of data points from Protocol 2 narrows with increasing system size, but the approximate linear relationship between the average z_J and ϕ_J is maintained. Images of five representative packings from the scatter plot in Fig. 2 are displayed in Fig. 3.

C. Compositional order

We now describe measurements of the compositional and positional order for static packings. For the compositional

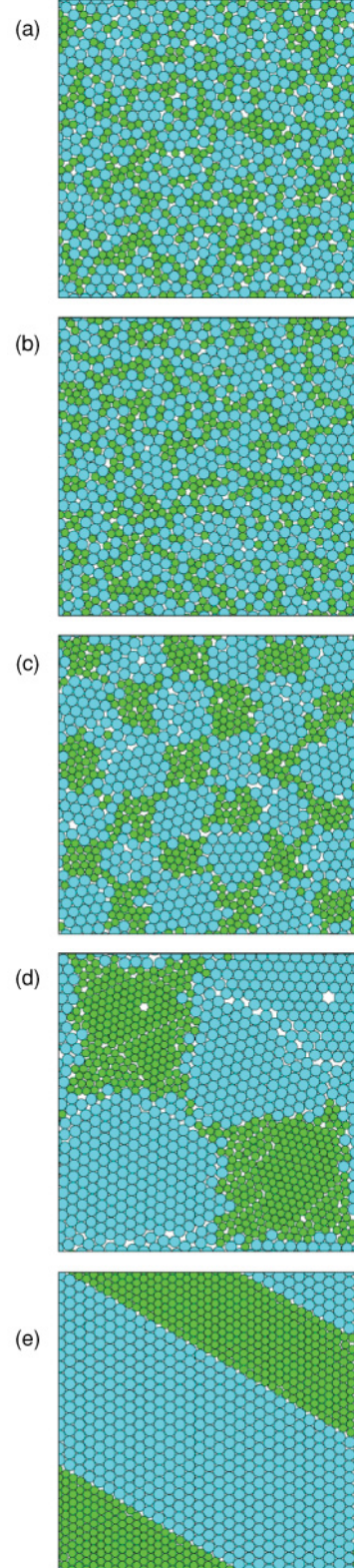


FIG. 3. (Color online) Images of representative static packings from the scatter plot in Fig. 2 with (a) $\phi_J = 0.837$, $z_J = 3.99$, (b) $\phi_J = 0.853$, $z_J = 4.00$, (c) $\phi_J = 0.846$, $z_J = 4.04$, (d) $\phi_J = 0.860$, $z_J = 4.41$, and (e) $\phi_J = 0.892$, $z_J \approx 4.1$. (See Appendix A.)

order, we quantify the fraction of overlapping pairs ($r_{ij} \leq \sigma_{ij}$) that involve two small f_{ss} or large f_{ll} particles or one small

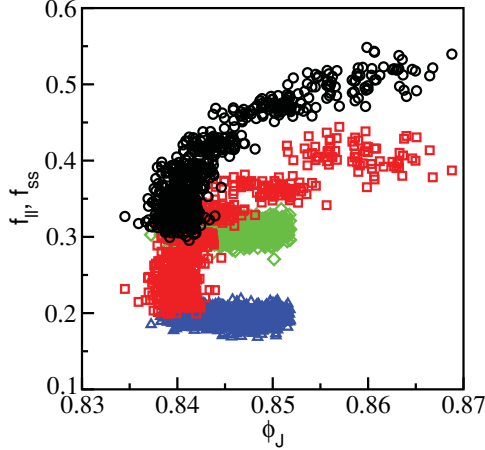


FIG. 4. (Color online) Scatter plot of the fraction of contacts between two large f_{ll} or two small particles f_{ss} versus packing fraction ϕ_J for all static packings from both protocols. The diamonds (circles) and triangles (squares) display data from Protocol 1 (2) for f_{ll} and f_{ss} , respectively.

and one large particle f_{sl} . A scatter plot of f_{ll} and f_{ss} versus ϕ_J for static packings generated from both protocols is shown in Fig. 4. The packings from Protocol 1 show no signs of complete phase separation with $f_{ss} + f_{ll} \approx f_{sl} \approx 0.5$ for all packings. However, when binned over narrow intervals of ϕ_J [Fig. 5(a)], f_{ll} shows a small systematic increase over the range of ϕ_J studied, which is consistent with results from Ref. [16]. In contrast, Protocol 2 generates static packings with a wide range of compositional order as shown in Figs. 3(c)–3(e). For example, at the largest ϕ_J , the system displays macrophase separation with $f_{ss} + f_{ll} \approx 1$ and $f_{sl} \approx 0$. We find similar results when we define contacting pairs as those with $r_{ij} \leq r_{\min}\sigma_{ij}$, where r_{\min} is set by the first minimum in $g(r)$.

D. Bond orientational order

To quantify positional order, we calculate the bond orientational order parameter ψ_6 , which measures the hexagonal registry of nearest neighbors [29]. ψ_6 can be calculated “locally,” which does not consider phase information, or “globally,” which allows phase cancellations. A polycrystal will yield a relatively large value for the local bond orientational order parameter ψ_6^l , even though the global order parameter $\psi_6^g \sim 1/\sqrt{N_d}$, where N_d is the number of polycrystalline domains. Equations (4) (global) and (5) (local) provide expressions for bond-orientational order parameters in 2D.

$$\psi_6^{\text{global}} = \frac{1}{N} \left| \sum_{k=1}^N \frac{1}{n_k} \sum_{j=1}^{n_k} e^{6i\theta_{kj}} \right|, \quad (4)$$

$$\psi_6^{\text{local}} = \frac{1}{N} \sum_{k=1}^N \frac{1}{n_k} \left| \sum_{j=1}^{n_k} e^{6i\theta_{kj}} \right|, \quad (5)$$

where θ_{kj} is the angle between a central particle k and neighbors j and n_k denotes the number of nearest neighbors of k . Two particles are deemed nearest neighbors if their center-to-center separation $r_{ij} < r_{\min}\sigma_{ij}$.

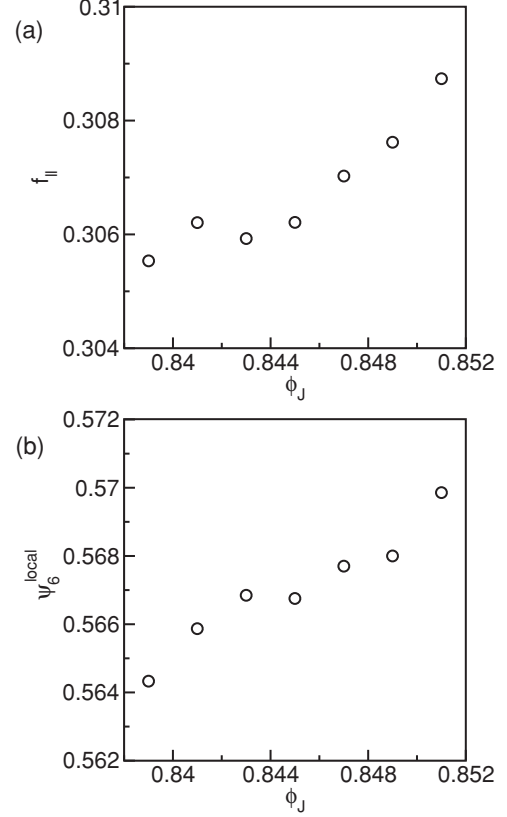


FIG. 5. (a) Fraction of contacts between two large particles f_{ll} and (b) local bond orientational order parameter ψ_6^{local} averaged over narrow bins in ϕ_J for Protocol 1.

The results for the global and local bond orientational parameters ψ_6^{global} and ψ_6^{local} are shown in Fig. 6. The static packings obtained from Protocol 1 possess only local bond orientational order with $\psi_6^{\text{local}} \approx 0.55$ as found in dense liquids [29] and $\psi_6^{\text{global}} \sim 1/\sqrt{N}$. Further, there is little correlation between the packing fraction ϕ_J and global or local bond

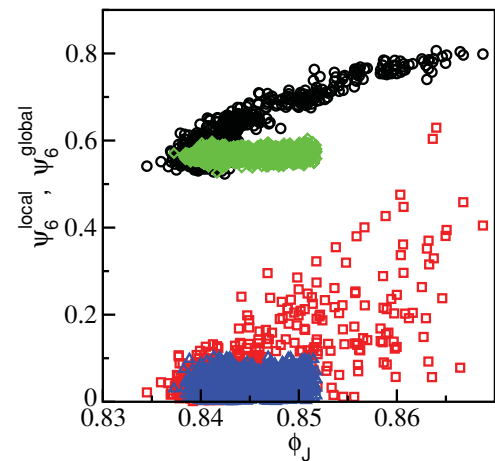


FIG. 6. (Color online) Scatter plot of local and global bond orientational order parameters, ψ_6^{local} and ψ_6^{global} , versus packing fraction ϕ_J for all static packings from both protocols. The diamonds (circles) and triangles (squares) display data from Protocol 1 (2) for ψ_6^{local} and ψ_6^{global} , respectively.

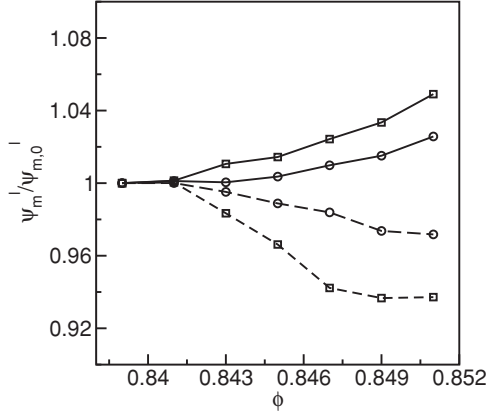


FIG. 7. Ratio of several local bond-orientational order parameters Ψ_m^l relative to their values $\Psi_{m,0}^l$ at the smallest ϕ_J obtained at large thermal quench rates for Protocol 1. The solid and dashed lines represent the order parameters ψ_6^l and ψ_4^s for definitions 1 (circles) and 2 (squares) for neighboring particles.

orientational order. When we average ψ_6^{local} over narrow bins in ϕ_J , we find that ψ_6^{local} increases weakly (less than $\approx 1\%$) with ϕ_J as shown in Fig. 5(b).

However, Fig. 3(b) indicates a propensity for small-scale clustering of large and small particles for $\phi_J > \phi_{\text{min}}$. Thus, we also studied order parameters (described in Appendix C) that are particularly sensitive to clustering in bidisperse systems [30]. As shown in Fig. 7, the most sensitive order parameters change by at most 5–6% over the range of ϕ_J obtained from Protocol 1. However, as discussed in Appendix D these packings with modest order obtained from Protocol 1 are still mechanically stable and isostatic.

In contrast, for the phase separated and partially crystalline packings from Protocol 2, we find that there is a strong positive correlation between ψ_6^{local} and ϕ_J and a somewhat weaker correlation between ψ_6^{global} and ϕ_J . Thus, we find that static packings from Protocols 1 and 2 have different structural properties. Those from Protocol 1 are largely disordered and possess similar structural properties even though they exist over a range of packing fraction. In contrast, there is a strong positive correlation between compositional and positional order and packing fraction for the phase-separated and partially crystalline packings from Protocol 2.

IV. MECHANICAL PROPERTIES

We will now describe the mechanical properties of the static packings, including the spectrum of normal modes from the dynamical matrix in the harmonic approximation and the static shear modulus as a function of contact number and order.

A. Spectrum of normal modes

The spectrum of normal modes provides significant insight into the structural and mechanical properties of mechanically stable packings [18]. For example, there is evidence that the low-frequency region of the spectrum controls the static shear response of jammed packings [31]. To calculate the spectrum, we diagonalize the dynamical matrix of all possible

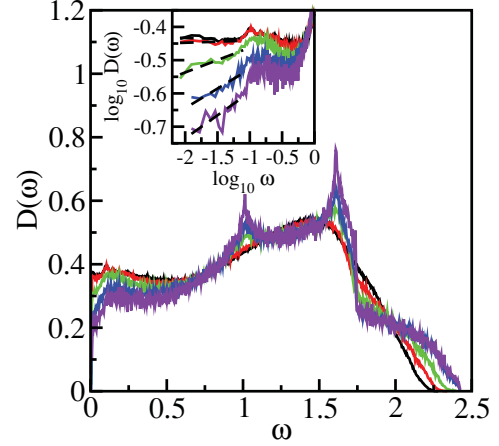


FIG. 8. (Color online) Density $D(\omega)$ of normal mode frequencies ω for $N = 1024$ bidisperse frictionless disk packings obtained using Protocols 1 and 2 as a function of the contact number at jamming onset for $z_J \simeq 4.0$ (black), $4.0 \leq z_J \leq 4.1$ (red), $4.1 \leq z_J \leq 4.2$ (green), $4.3 \leq z_J \leq 4.4$ (blue), and $4.5 \leq z_J \leq 4.6$ (violet), from top to bottom, at low frequencies. The inset shows the same data except that it focuses on low frequencies $\omega < 1$ and includes power-law fits to $D(\omega) \sim \omega^\alpha$ as dashed lines.

second derivatives of the potential energy with respect to particle positions evaluated at positions of the static packing—assuming that no existing contacts break and no new contacts form [32]. This yields $2N' - 2$ nontrivial eigenvalues e_i after accounting for translational invariance. We focus on mechanically stable packings, where (nearly) all $2N' - 2$ of the eigenvalues are nonzero [33]. (See Appendix D.)

The density $D(\omega)$ of normal mode frequencies $\omega_i = \sqrt{e_i/N}$, or density of states (DOS), is given by $D(\omega) = [N(\omega + \delta\omega) - N(\omega)]/\delta\omega$, where $N(\omega)$ is the number of modes with frequency less than or equal to ω . The density of states $D(\omega)$ for packings of bidisperse frictionless disks is shown in Fig. 8 as a function of the contact number at jamming onset z_J . As in previous studies [18], we find that for isostatic systems with $z_J \simeq 4$, $D(\omega)$ possesses a nearly constant regime at low frequencies, which signals an abundance of low-frequency modes compared to ideal Debye behavior [where $D(\omega) \sim \omega$ as $\omega \rightarrow 0$] for ideal 2D harmonic solids. For the micro- and macro-phase separated bidisperse packings generated using Protocol 2 with $z_J \gtrsim 4.1$, the density of states develops two other interesting features. First, $D(\omega)$ develops two strong peaks near $\omega \simeq 1.0$ and 1.6 instead of a single broad peak centered near $\omega \approx 1.4$ for isostatic amorphous systems. (We will see below that these peaks are associated with crystallization.) Second, we observe that as z_J increases and the packings become hyperstatic, the weight in $D(\omega)$ at low frequency ($\omega \lesssim 0.3$) decreases. As shown in the inset to Fig. 8, the density of states scales as a power law

$$D(\omega) \sim \omega^\alpha \quad (6)$$

in the limit $\omega \rightarrow 0$ with a scaling exponent α that varies continuously with contact number z_J as shown in Fig. 9. (See Appendix B for a discussion of the system-size dependence of the exponent α .) Note, however, that the plateau in the density of states remains largely unchanged in the intermediate

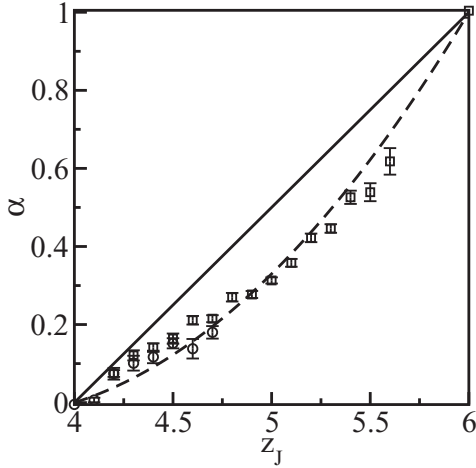


FIG. 9. Power-law exponent α for the scaling of the density of normal modes with frequency in the limit $\omega \rightarrow 0$ [$D(\omega) \sim \omega^\alpha$] as a function of contact number at jamming onset z_J for bidisperse (circles) and monodisperse (squares) packings. (The error bars indicate the error in α from least-squares analysis.) The dashed line is a fit to Eq. (7) (with $c = 0.17$), which interpolates the data between the limiting values $\alpha = 0$ at $z_J = z_{\text{iso}} = 4$ and $\alpha = 1$ (Debye behavior) at $z_J = z_{\text{xtal}} = 6$. The solid line is Eq. (7) with $c = 0$.

frequency regime $0.3 \leq \omega \lesssim 1$ over a wide range of z_J , which implies that some of the remarkable features of jamming in isostatic systems also hold for hyperstatic systems.

To test the generality of the results for the density of states, we also calculated $D(\omega)$ for monodisperse frictionless disk packings generated using Protocol 1 as shown in Fig. 10. The density of states for monodisperse systems displays similar features to that for bidisperse systems. (i) A plateau in $D(\omega)$ exists at low to intermediate frequencies for nearly isostatic systems. (ii) Strong distinct peaks are located near $\omega \simeq 1.4$ and

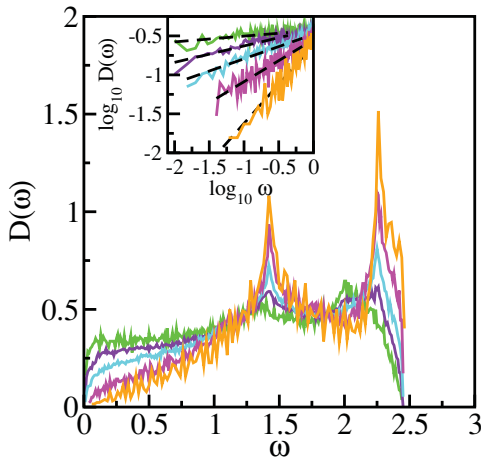


FIG. 10. (Color online) Density $D(\omega)$ of normal mode frequencies ω for $N = 1024$ monodisperse frictionless disk packings obtained using Protocol 1 as a function of the contact number at jamming onset for $4.1 \leq z_J \leq 4.2$ (green), $4.5 \leq z_J \leq 4.6$ (violet), $4.9 \leq z_J \leq 5.0$ (cyan), $5.4 \leq z_J \leq 5.5$ (magenta), and $z_J \simeq 6.0$ (orange), from top to bottom, at low frequencies. The inset shows the same data except that it focuses on low frequencies $\omega < 1$ and includes power-law fits to $D(\omega) \sim \omega^\alpha$ as dashed lines.

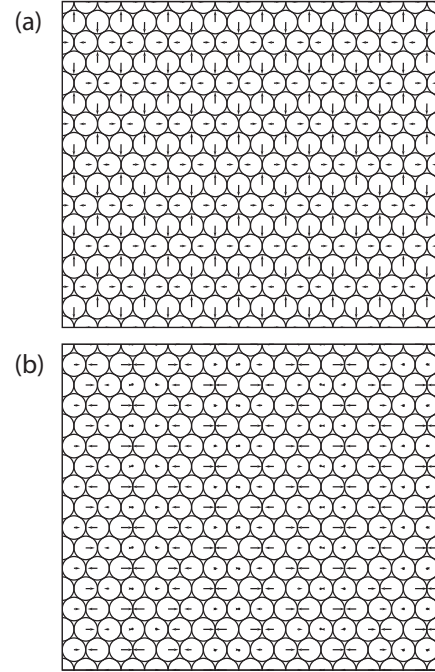


FIG. 11. Eigenvectors corresponding to the modes with frequencies near the (a) first and (b) second peaks in the density of states $D(\omega)$ for monodisperse packings with $z_J \simeq 6$ and $\phi_J \simeq \phi_{\text{xtal}}$ for $N = 256$. The size of the eigenvector component for each particle is proportional to the length of the vector displacement associated with each particle.

2.25 for hyperstatic packings. Eigenvectors that correspond to the two peak frequencies are visualized in Fig. 11. (iii) A power-law regime $D(\omega) \sim \omega^\alpha$ develops in the $\omega \rightarrow 0$ limit for hyperstatic packings. The exponent α varies continuously with z_J with a similar functional dependence to that for bidisperse systems as shown in Fig. 9. A notable difference between bidisperse and monodisperse systems is that a continuous power-law regime in $D(\omega)$ persists to higher frequencies ($\omega \sim 1$) for monodisperse compared to bidisperse systems.

The dependence of the scaling exponent α on z_J is displayed for all bidisperse and monodisperse packings (binned by z_J) in Fig. 9. We find that α increases monotonically with z_J and use the suggestive empirical form

$$\alpha = (d - 1) \frac{z_J - z_{\text{iso}}}{z_{\text{xtal}} - z_{\text{iso}}} + c(z_J - z_{\text{iso}})(z_J - z_{\text{xtal}}), \quad (7)$$

where c is a fitting parameter to describe the data between the limiting values $\alpha = 0$ at $z_J = z_{\text{iso}}$ and $\alpha = d - 1$ (Debye behavior) at $z_J = z_{\text{xtal}}$. The continuous increase in α from 0 to 1 as the contact number increases suggests a different scenario for the behavior of the jamming transition as a function of z_J and positional order compared to the discontinuous changes in the structural properties of frictional granular systems when they are compacted above random close packing [34,35]. More work needs to be done to understand how key differences in these studies (spatial dimensionality, frictional interactions, and packing protocols) affect the evolution in the positional order with contact number in jammed packings.

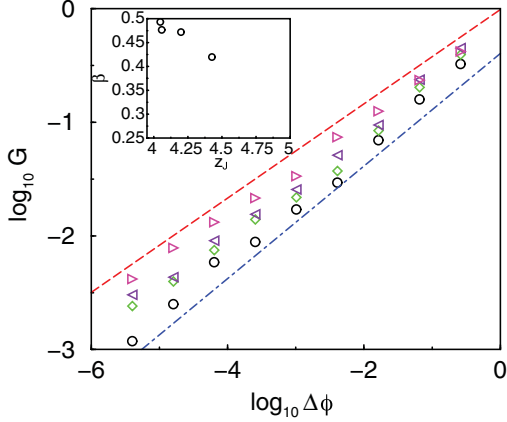


FIG. 12. (Color online) Static shear modulus G versus the deviation in packing fraction from the jamming onset $\Delta\phi = \phi - \phi_J$ for static packings at $(z_J) = 4.0$ (circles), 4.15 (diamonds), 4.35 (left triangles), and 4.55 (right triangles). The long dashed (dot-dashed) line has slope 0.4 (0.5). The inset shows the power-law scaling exponent β for the static shear modulus [$G \sim (\Delta\phi)^\beta$] versus the contact number z_J at jamming.

B. Static shear modulus

To measure the static linear shear modulus G , we slightly deform the system by applying an infinitesimal simple shear strain γ (along the x direction with gradient in the y direction), allowing the system to relax via energy minimization at fixed strain, and then measuring the resulting shear stress response, $G = d\Sigma_{xy}/d\gamma$. In Fig. 12, we show the shear modulus versus the amount of compression $\Delta\phi = \phi - \phi_J$ for bidisperse packings obtained from Protocols 1 and 2 at several values of z_J . We find generally that in the limit $\Delta\phi \rightarrow 0$ the static shear modulus scales as a power law with $\Delta\phi$:

$$G = G_0(\Delta\phi)^\beta, \quad (8)$$

where the scaling exponent β (and prefactor G_0) depend on z_J . As shown in Fig. 12, β decreases steadily from 0.5 to 0.4 as the contact number z_J at jamming increases. Note that $\beta = 0.5$ for $z_J = z_{\text{iso}}$ was obtained in previous work on isostatic packings [18]. The results in Fig. 12 suggest that the critical behavior (e.g., power-law scaling of the shear modulus) found in jammed isostatic systems persists when the jamming onset is hyperstatic. Further studies are required to determine whether the scaling exponent for the static shear modulus can be varied over the full range from 0.5 to 0.

V. CONCLUSIONS

Using computer simulations, we generated a large library of mechanically stable packings of bidisperse, frictionless disks that span a wide range of contact number from $z_J = z_{\text{iso}} = 4$ to $z_{\text{xtal}} = 6$ and packing fraction at jamming from $\phi_J \sim 0.84$ to near ϕ_{xtal} . We find that there is a disordered, isostatic branch of MS packings that spans a finite range in packing fraction in the large-system limit. Over this range of packing fraction, these packings are disordered with only weak correlations between bond orientational order, clustering propensity, compositional order, and ϕ_J . Further studies need to be performed to pin down the upper bound in ϕ_J for the disordered, isostatic branch of MS packings. We also find a branch of phase-separated and

partially crystalline packings for which the compositional and positional order increase with ϕ_J . In addition, we characterize the mechanical properties of the static packings by measuring the spectrum of normal modes in the harmonic approximation and the static shear modulus. We find that the mechanical properties of the packings vary *continuously* as the contact number and structural and compositional order at jamming onset increase from their isostatic values. In particular, we find that the static shear modulus scales as a power law in the amount of compression, $G \sim (\Delta\phi)^\beta$, and that the low-frequency density of states scales as a power law in frequency, $D(\omega) \sim \omega^\alpha$, and both α and β vary continuously with contact number at jamming onset. These findings emphasize that jamming behavior in systems with purely repulsive contact potentials occurs over a range of contact numbers, not just near $z_J = z_{\text{iso}}$ [36–38]. In future studies, we will investigate the relationship between the scaling exponents α and β , which is likely an important feature of jamming in hyperstatic systems.

ACKNOWLEDGMENTS

We thank the organizers of the Frontiers in Nonequilibrium Physics and YKIS2009 workshops. We also acknowledge A. Donev, R. Hoy, and M. Shattuck for helpful conversations. This research was supported by the National Science Foundation under Grants No. CBET-0828359 (LS), No. DMS-0835742 (CO, CS), and No. PHY-0551164. We thank the Kavli Institute for Theoretical Physics for their hospitality during “The Physics of Glasses: Relating Metallic Glasses to Molecular, Polymeric and Oxide Glasses” Program. This work also benefited from the facilities and staff of the Yale University Faculty of Arts and Sciences High Performance Computing Center and NSF Grant No. CNS-0821132 that partially funded acquisition of the computational facilities.

APPENDIX A: ERROR ANALYSIS OF CONTACT NUMBER

In this Appendix, we study how sensitive the contact number z_J is to the definition of whether two particles are in contact. In Fig. 13, we show z_J versus $\log_{10} a$ where two

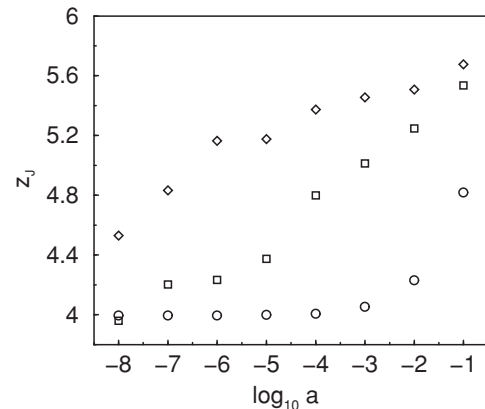


FIG. 13. The contact number z_J as a function of a , where the condition $r_{ij} \leq (1+a)\sigma_{ij}$ determines whether particles i and j are in contact. The packings shown are $N = 1024$, $\phi_J = 0.837$ (circles); $N = 1014$, $\phi_J = 0.892$ (squares); and $N = 2390$, $\phi_J = 0.897$ (diamonds).

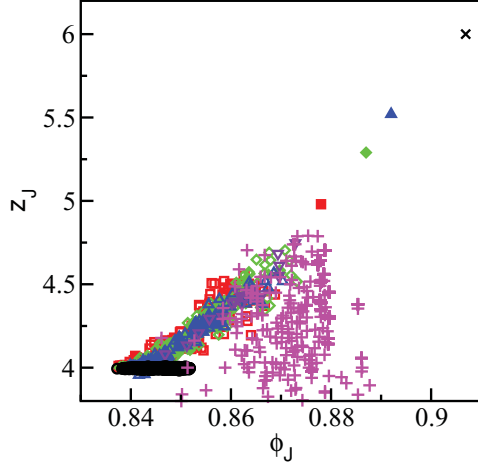


FIG. 14. (Color online) Contact number z_J versus packing fraction ϕ_J for the same data in Fig. 2 and an additional set of packings obtained from thermalizing the configurations in Fig. 2 with $\phi_J > 0.86$ and then identifying the nearest packing. The variation in z_J increases with ϕ_J .

disks i and j are considered in contact (or overlapping) if $r_{ij} \leq (1 + a)\sigma_{ij}$ for three representative configurations: $N = 1024$, $\phi_J = 0.837$ (circles); $N = 1014$, $\phi_J = 0.892$ (squares); and $N = 2390$, $\phi_J = 0.897$ (diamonds). We see that the contact number is well defined for amorphous configurations at low packing fractions, i.e., the contact number is constant over a wide range of a that determines whether two particles are in contact. In contrast, for packings with large ϕ_J and significant order as shown in Fig. 3(e), the contact number varies continuously with a down to the numerical precision of the particle positions in the simulations. Thus, at the current numerical precision of the simulations, it is difficult to determine z_J accurately for the partially ordered and ordered configurations. To test the robustness of the contact numbers, we also added weak thermal fluctuations to the packings with $\phi_J > 0.855$ in Fig. 2 for times significantly shorter than the structural relaxation time and then found the nearest static jammed packing. These data, shown by the small solid symbols in Fig. 14, possess surprisingly small contact numbers and begin to fill in the region at large ϕ_J and small z_J . As a result, we only include configurations in Fig. 2 that possess plateaus in z_J versus a over a range $a_{\min} \leq a \leq a_{\max}$ of at least two orders of magnitude with $a_{\min} \geq 10^{-8}$.

APPENDIX B: ROBUSTNESS OF THE DENSITY OF STATES

In this Appendix, we test the robustness of our measurements of the density of states $D(\omega)$ by (1) studying the system-size dependence of the accumulated frequency distribution $N(\omega)$ and (2) comparing $D(\omega)$ for hyperstatic packings at jamming onset with contact number z_J to that for overcompressed packings at the same contact number $z = z_J$.

To eliminate noise from numerical differentiation, we calculate the accumulated distribution $N(\omega) = \int_0^\omega D(\omega')d\omega'$ (number of modes with frequency less than or equal to ω). For reference, in Fig. 15, we show $N(\omega)$ for monodisperse packings at jamming onset with $z_J \simeq 6$ and $\phi_J \simeq \phi_{\text{xtal}}$ as a function of system size for $N = 16$ to 6400. The crystalline

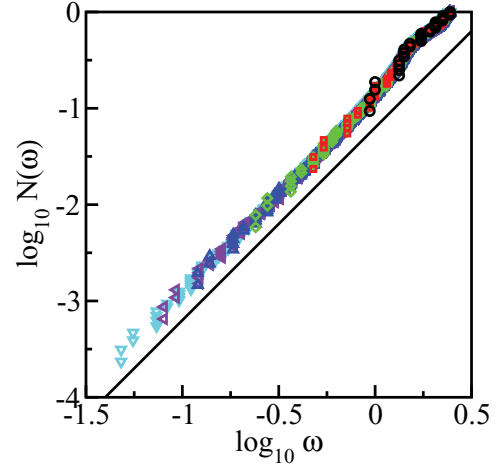


FIG. 15. (Color online) Number $N(\omega)$ of normal modes of the dynamical matrix with frequency less than or equal to ω for monodisperse packings at jamming onset with $z_J \simeq 6$ and $\phi_J \simeq \phi_{\text{xtal}}$ and $N = 16$ (circles), 64 (squares), 256 (diamonds), 1024 (upward triangles), 2304 (leftward triangles), and 6400 (downward triangles). The solid line has slope 2.

systems show robust Debye power-law scaling $N(\omega) \sim \omega^2$ at low frequency for all system sizes. $N(\omega)$ for bidisperse packings at jamming onset is shown in Fig. 16 for $4.4 \leq z_J \leq 4.5$ as a function of system size. $N(\omega)$ displays a power-law scaling with an exponent that approaches $1 + \alpha = 1.16 > 1$ in the large-system limit. Similar robust scaling exponents are found for all z_J .

Distinctive features of the density of states $D(\omega)$ for hyperstatic bidisperse packings at jamming onset are the power-law scaling of $D(\omega) \sim \omega^\alpha$ at the lowest frequencies, where α varies continuously with z_J , and the persistence of the plateau in $D(\omega)$ at intermediate frequencies over a range of z_J . Do highly compressed packings display

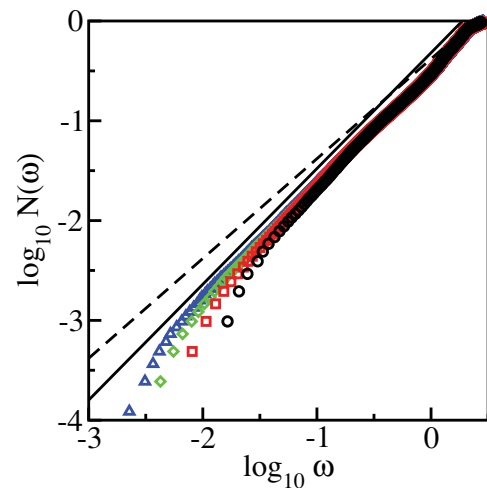


FIG. 16. (Color online) Number $N(\omega)$ of normal modes of the dynamical matrix with frequency less than or equal to ω for bidisperse packings at jamming onset generated using Protocol 2 with $4.4 \leq z_J \leq 4.5$ and $N = 512$ (circles), 1024 (squares), 2048 (diamonds), and 4096 (triangles). The solid (dashed) line has slope 1.16 (1).

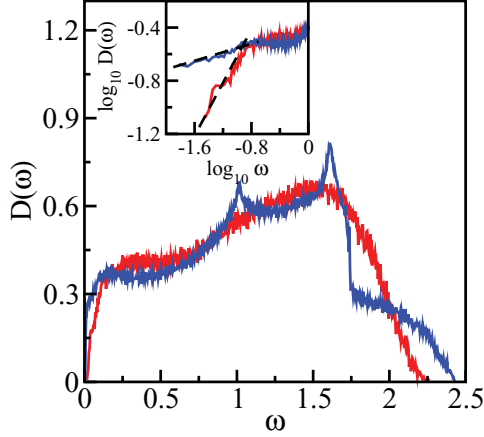


FIG. 17. (Color online) The density of normal modes $D(\omega)$ with frequency ω for bidisperse packings at jamming onset generated using Protocol 2 with $4.4 \leq z_J \leq 4.5$ (blue) and overcompressed packings with contact number z in the same range (red), from top to bottom, at low frequency. The dashed lines in the inset have slope 0.16 and 1.

these same features? In Fig. 17, we compare $D(\omega)$ for hyperstatic packings at jamming onset with $4.4 \leq z_J \leq 4.5$ and overcompressed packings in the same range of contact number $z \sim z_J$. For the overcompressed packings, we find that $D(\omega) \sim \omega^\alpha$, with $\alpha = 1$, while $\alpha \approx 0.16$ at the lowest frequencies with a crossover to a plateau at intermediate frequencies for the hyperstatic packings at jamming onset. Thus, hyperstatic packings at jamming onset possess significantly more low-frequency normal modes than overcompressed systems at the same contact number as shown in the inset to Fig. 17.

APPENDIX C: EVOLUTION OF STRUCTURAL PROPERTIES WITH ϕ_J

In this Appendix, we complement the scatter plots of the structural and mechanical properties in Secs. III and IV by showing how these quantities averaged over narrow bins in ϕ_J vary with packing fraction for packings generated using Protocol 1. We find that the averaged quantities display small systematic increases or decreases with ϕ_J , typically several percentage points or less. In Fig. 5, we show the average (a) fraction of large-large contacts f_{ll} and (b) local bond orientational order parameter ψ_6^{local} as a function of ϕ_J . Both quantities show a $\approx 1\%$ increase over the range $\phi_J = \phi_{\text{min}}$ to ϕ_{max} ($r = 10^{-6}$). Both f_{ss} and ψ_6^{global} show less systematic dependence on ϕ_J than f_{ll} and ψ_6^{local} .

In Fig. 18, we show [Fig. 18(a)] the pair correlation between large particles $g_{ll}(r)$ and [Fig. 18(b)] density of normal mode frequencies $D(\omega)$ for $\phi_J \approx 0.84$, $0.842 \leq \phi_J \leq 0.844$, $0.846 \leq \phi_J \leq 0.848$, and $\phi_J \geq 0.85$. We find only subtle changes in both quantities with increasing ϕ_J . The peaks in $g_{ll}(r)$ grow and minima become deeper and shift to slightly larger separations r/σ_l with increasing ϕ_J as shown previously for 3D bidisperse frictionless packings [15]. Similarly, we find only a small change in the peak height near $\omega = 1.5$ in the density of normal modes with increasing ϕ_J .

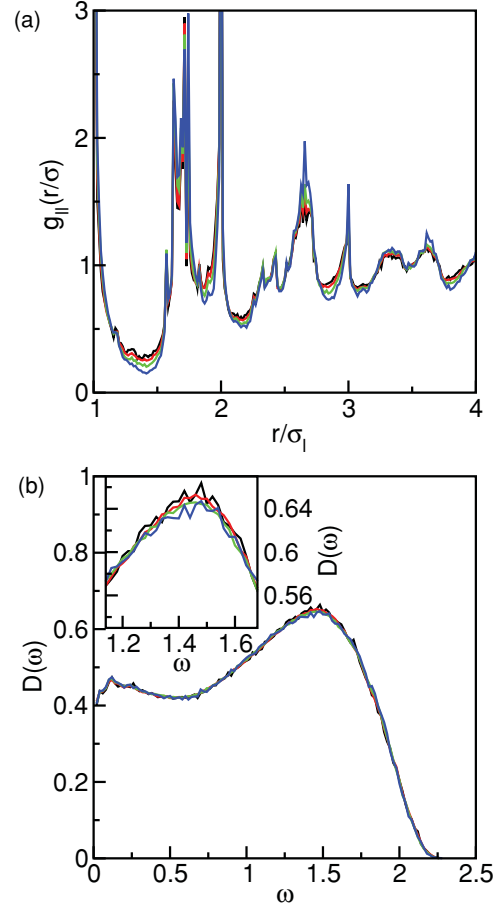


FIG. 18. (Color online) (a) Pair correlation function between large particles $g_{ll}(r)$ as a function of separation r/σ_l and (b) density $D(\omega)$ of normal mode frequencies ω using Protocol 1 for $\phi_J \leq 0.84$ (black), $0.842 \leq \phi_J \leq 0.844$ (red), $0.846 \leq \phi_J \leq 0.848$ (green), and $\phi_J \geq 0.85$ (blue), from top to bottom, near the first minimum in $g(r)$ in (a) and near the strong peak in $D(\omega)$ in (b). The inset to (b) magnifies the peak in $D(\omega)$ near $\omega = 1.5$.

We have also studied more general bond orientational order parameters in which we distinguish among large-large, small-large, and large-large contacts to detect clustering of large or small particles. We calculated several classes of local bond orientational order parameters:

$$\psi_m^l = \frac{1}{N_l} \sum_{k=1}^{N_l} \frac{1}{n_k} \left| \sum_{j=1}^{n_k} e^{im\theta_{kj}} \right|, \quad (\text{C1})$$

$$\psi_m^s = \frac{1}{N_s} \sum_{k=1}^{N_s} \frac{1}{n_k} \left| \sum_{j=1}^{n_k} e^{im\theta_{kj}} \right|, \quad (\text{C2})$$

$$\psi_m^{ll} = \frac{1}{N_l} \sum_{k=1}^{N_l} \frac{1}{n_k^l} \left| \sum_{j=1}^{n_k^l} e^{im\theta_{kj}} \right|, \quad (\text{C3})$$

$$\psi_m^{ls} = \frac{1}{N_l} \sum_{k=1}^{N_l} \frac{1}{n_k^s} \left| \sum_{j=1}^{n_k^s} e^{im\theta_{kj}} \right|, \quad (\text{C4})$$

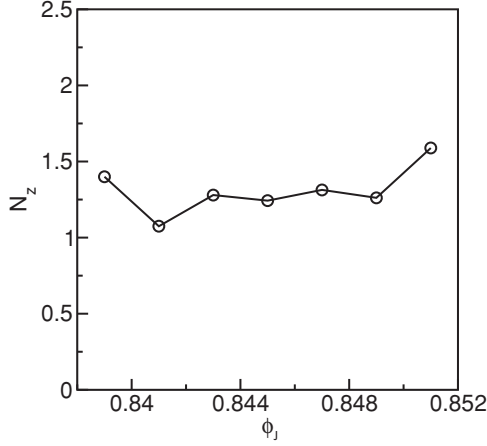


FIG. 19. Average number of nontrivial zero eigenvalues N_z of the dynamical matrix for static packings generated from Protocol 1 as a function of ϕ_J .

and

$$\psi_m^{ss} = \frac{1}{N_s} \sum_{k=1}^{N_s} \frac{1}{n_k^s} \left| \sum_{j=1}^{n_k^s} e^{im\theta_{kj}} \right|, \quad (\text{C5})$$

where $m = 2, 4, \text{ and } 6$ and N_s (N_l) is the number of small (large) particles. For ψ_m^l , the first sum over k includes only large particles and the second sum over neighboring particles j includes both large and small particles. For ψ_m^s , the first sum includes only small particles and the second sum over neighboring particles j includes both large and small particles. For ψ_m^{ll} , the first and second sums include only large particles. Similar definitions are used for ψ_m^{ls} , ψ_m^{sl} , and ψ_m^{ss} . We also calculated the corresponding global versions of these order parameters and defined neighboring particles as (i) contacting (or infinitesimally overlapping) particle pairs or (ii) particle pairs with separations less than the location of the first minimum in $g(r)$. As shown in Fig. 7, over the full range of packing fractions obtained from Protocol 1, the largest decrease in the order parameters [Eqs. (C1)–(C5)] occurs in ψ_4^s (between 4 and 6%) and the largest increase occurs in

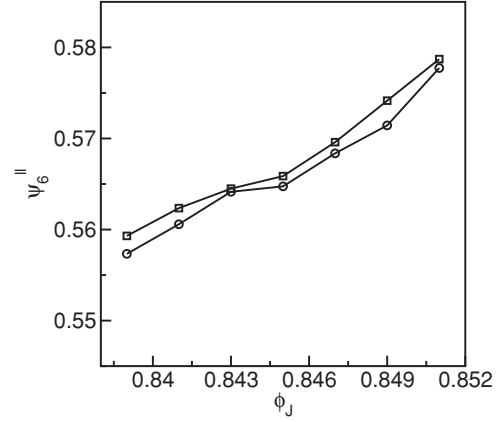


FIG. 20. Bond orientational order parameter ψ_6^{ll} versus ϕ_J for packings obtained from Protocol 1 with no nontrivial zero eigenvalues of the dynamical matrix (circles) and a small number of nontrivial zero eigenvalues (squares).

ψ_6^{ll} (between 2 and 4%), which are larger than the changes (-2%) in f_{ll} and ψ_6^{local} in Figs. 5(a) and 5(b).

APPENDIX D: MECHANICAL STABILITY

Static packings are isostatic if they are mechanically stable [i.e., all nonrattler particles in the packing are in force balance, and the number of nonzero eigenvalues of the dynamical matrix $N_n = N_n^* \equiv d(N - N_r) - d$, where d is the spatial dimension], and if they possess only the minimum number of distinct contacts $N_c = N_c^{\text{min}} \equiv N_n^* + 1$ required for stability. In Fig. 19, we plot the average number of nontrivial zero eigenvalues of the dynamical matrix N_z versus packing fraction for packings generated from Protocol 1. Most static packings from Protocol 1 are mechanically stable; the average number of zero modes is roughly 1 out of $2N$ modes independent of ϕ_J . In Fig. 20, we show that the small number of nontrivial zero modes present in the packings from Protocol 1 does not strongly affect their structural properties. ψ_6^{ll} versus ϕ_g is nearly the same for static packings with and without nontrivial zero eigenvalues of the dynamical matrix.

-
- [1] F. H. Stillinger, *Science* **267**, 1935 (1995).
 [2] N. Xu, J. Blawdziewicz, and C. S. O'Hern, *Phys. Rev. E* **71**, 061306 (2005).
 [3] G.-J. Gao, J. Blawdziewicz, and C. S. O'Hern, *Phys. Rev. E* **74**, 061304 (2006).
 [4] C. Song, P. Wang, and H. A. Makse, *Nature* **453**, 629 (2008).
 [5] F. H. Stillinger, *Phys. Rev. E* **59**, 48 (1999).
 [6] G.-J. Gao, J. Blawdziewicz, C. S. O'Hern, and M. Shattuck, *Phys. Rev. E* **80**, 061304 (2009).
 [7] S. Torquato, T. M. Truskett, and P. G. Debenedetti, *Phys. Rev. Lett.* **84**, 2064 (2000).
 [8] A. R. Kansal, S. Torquato, and F. H. Stillinger, *Phys. Rev. E* **66**, 041109 (2002).
 [9] M. D. Rintoul and S. Torquato, *Phys. Rev. Lett.* **77**, 4198 (1996).
 [10] B. D. Lubachevsky, F. H. Stillinger, and E. N. Pinson, *J. Stat. Phys.* **64**, 501 (1991).
 [11] A. V. Tkachenko and T. A. Witten, *Phys. Rev. E* **60**, 687 (1999).
 [12] A. Donev, F. H. Stillinger, and S. Torquato, *Phys. Rev. Lett.* **96**, 225502 (2006).
 [13] M. P. Ciamarra, M. Nicodemi, and A. Coniglio, *Soft Matter* **6**, 2871 (2010).
 [14] M. Hermes and M. Dijkstra, *Europhys. Lett.* **89**, 38005 (2010).
 [15] P. Chaudhuri, L. Berthier, and S. Sastry, *Phys. Rev. Lett.* **104**, 165701 (2010).
 [16] D. Vågberg, P. Olsson, and S. Teitel, *Phys. Rev. E* **83**, 031307 (2011).

- [17] F. Lechenault, O. Dauchot, G. Biroli, and J.-P. Bouchaud, *Europhys. Lett.* **83**, 46003 (2008).
- [18] C. S. O'Hern, L. E. Silbert, A. J. Liu, and S. R. Nagel, *Phys. Rev. E* **68**, 011306 (2003).
- [19] R. D. Kamien and A. J. Liu, *Phys. Rev. Lett.* **99**, 155501 (2007).
- [20] A. J. Liu, M. Wyart, W. van Saarloos, and S. R. Nagel, in *Dynamical Heterogeneities and Glasses*, edited by L. Cipeletti *et al.* (Oxford University Press, Oxford, UK, 2010).
- [21] L. E. Silbert, A. J. Liu, and S. R. Nagel, *Phys. Rev. Lett.* **95**, 098301 (2005).
- [22] X. Mao, N. Xu, and T. C. Lubensky, *Phys. Rev. Lett.* **104**, 085504 (2010).
- [23] S. Torquato and F. H. Stillinger, *J. Phys. Chem. B* **105**, 11849 (2001).
- [24] Note that we create hyperstatic packings at jamming onset, i.e., in the limit where particle overlap is reduced to zero. Our studies differ from those that generate hyperstatic packings by compressing the system [18].
- [25] D. N. Perera and P. Harrowell, *Phys. Rev. E* **59**, 5721 (1999).
- [26] O. U. Uche, F. H. Stillinger, and S. Torquato, *Physica A* **342**, 428 (2004).
- [27] W. Kob and H. C. Andersen, *Phys. Rev. E* **52**, 4134 (1995).
- [28] We assume that the largest packing fraction in bidisperse systems is the macrophase-separated packing with $\phi_J \approx \phi_{\text{staj}}$ in the large-system limit.
- [29] P. J. Steinhardt, D. R. Nelson, and M. Ronchetti, *Phys. Rev. B* **28**, 784 (1983).
- [30] F. Ebert, P. Keim, and G. Maret, *Eur. Phys. J. E* **26**, 161 (2008).
- [31] M. Mailman, C. F. Schreck, C. S. O'Hern, and B. Chakraborty, *Phys. Rev. Lett.* **102**, 255501 (2009).
- [32] C. F. Schreck and C. S. O'Hern, in *Experimental and Computational Techniques in Soft Condensed Matter Physics*, edited by J. S. Olafsen (Cambridge University Press, New York, 2010).
- [33] We use a threshold of $e_{\min} = 10^{-6}$ above which eigenvalues are deemed nonzero.
- [34] Y. Jin and H. A. Makse, *Physica A* **389**, 5362 (2010).
- [35] C. Radin, *J. Stat. Phys.* **131**, 567 (2008).
- [36] T. Hatano, M. Otsuki, and S. Sasa, *J. Phys. Soc. Jpn.* **76**, 023001 (2007).
- [37] T. Hatano, *J. Phys. Soc. Jpn.* **77**, 123002 (2008).
- [38] M. Otsuki and H. Hayakawa, *Prog. Theor. Phys.* **121**, 647 (2009).